K2-265 b: a transiting rocky super-Earth

K. W. F. Lam[1],[*], A. Santerne[2], S. G. Sousa[3], A. Vigan[2], D. J. Armstrong[1],[4], S. C. C. Barros[3], B. Brugger[2], V. Adibekyan[3],
J.-M. Almenara[5], E. Delgado Mena[3], X. Dumusque[5], D. Barrado[6], D. Bayliss[1], A. S. Bonomo[7], F. Bouchy[5],
D. J. A. Brown[1],[4], D. Ciardi[8], M. Deleuil[2], O. Demangeon[3], F. Faedi[9],[1], E. Foxell[1], J. A. G. Jackman[1],[4], G. W. King[1],
J. Kirk[1], R. Ligi[2], J. Lillo-Box[10], T. Lopez[2], C. Lovis[5], T. Louden[1],[4], L. D. Nielsen[5], J. McCormac[1],[4],
O. Mousis[2], H. P. Osborn[2], D. Pollacco[1],[4], N. C. Santos[3],[11], S. Udry[5], and P. J. Wheatley[1],[4]

[1] Department of Physics, University of Warwick, Gibbet Hill Road, Coventry, CV4 7AL, UK
   e-mail: w.f.lam@warwick.ac.uk
[2] Aix Marseille University, CNRS, CNES, LAM, Marseille, France
[3] Instituto de Astrofísica e Ciências do Espaço, Universidade do Porto, CAUP, Rua das Estrelas, 4150-762 Porto, Portugal
[4] Centre for Exoplanets and Habitability, University of Warwick, Gibbet Hill Road, Coventry CV4 7AL, UK
[5] Observatoire Astronomique de l'Université de Genève, 51 Chemin des Maillettes, 1290 Versoix, Switzerland
[6] Departamento de Astrofísica, Centro de Astrobiología (CSIC-INTA), ESAC campus 28692 Villanueva de la Cañada (Madrid),
   Spain
[7] INAF – Osservatorio Astrofisico di Torino, Strada Osservatorio 20, 10025, Pino Torinese (TO), Italy
[8] Caltech/IPAC-NASA Exoplanet Science Institute, 770 S. Wilson Ave, Pasadena, CA 91106, USA
[9] INAF – Osservatorio Astrofisica di Catania, Via S. Sofia 78, 95123, Catania Italy
[10] European Southern Observatory (ESO), Alonso de Cordova 3107, Vitacura, Casilla 19001, Santiago de Chile, Chile
[11] Departamento de Física e Astronomia, Faculdade de Ciencias, Universidade do Porto, Rua Campo Alegre, 4169-007 Porto,
   Portugal

ABSTRACT

We report the discovery of the super-Earth K2-265 b detected with *K2* photometry. The planet orbits a bright (V_{mag} = 11.1) star of spectral type G8V with a period of 2.37 days. We obtained high-precision follow-up radial velocity measurements from HARPS, and the joint Bayesian analysis showed that K2-265 b has a radius of $1.71 \pm 0.11\ R_\oplus$ and a mass of $6.54 \pm 0.84\ M_\oplus$, corresponding to a bulk density of $7.1 \pm 1.8\ \mathrm{g\ cm^{-3}}$. Composition analysis of the planet reveals an Earth-like, rocky interior; this object has a rock mass fraction of ~80%. The short orbital period and small radius of the planet puts it below the lower limit of the photoevaporation gap, where the envelope of the planet could have eroded owing to strong stellar irradiation, leaving behind an exposed core. Knowledge of the planet core composition allows us to infer the possible formation and evolution mechanism responsible for its current physical parameters.

Key words. techniques: photometric – techniques: radial velocities – planets and satellites: detection – stars: individual: K2-265 – planets and satellites: composition

1. Introduction

Exoplanetary discovery has widened our perspective and knowledge of planetary science in the past two decades. The space-based mission *Kepler* used transit photometry to detect and characterise exoplanets (Borucki et al. 2010, 2011; Koch et al. 2010) and one of its key objectives is the determination of the frequency of terrestrial planets in the habitable zones of stars. From their sample of over 4000 transiting planet candidates, it was revealed that small planets ($R_P < 4.0\ R_\oplus$) are by far the most common in our Galaxy (Howard et al. 2012; Batalha et al. 2013; Dressing & Charbonneau 2013; Petigura et al. 2013); this result is also supported by radial velocity (RV) surveys (e.g. Mayor et al. 2011; Bonfils et al. 2013). While the *Kepler* sample provided an insight into the planet occurrence rate (e.g. Batalha 2014), only a few dozen host stars were bright enough for follow-up characterisation. With the loss of two reaction wheels on the *Kepler*

spacecraft, the *K2* mission was adopted to extend the transiting exoplanet discoveries (Howell et al. 2014). The *K2* mission has observed 19 fields so far and has supplied precise photometry of approximately 20 000 bright stars per campaign. This has yielded hundreds of transiting planet candidates (e.g. Vanderburg et al. 2016; Barros et al. 2016; Pope et al. 2016), over 300 of which have been statistically validated (e.g. Montet et al. 2015; Barros et al. 2015; Crossfield et al. 2016).

Super-Earths are absent in our own solar system. Therefore, they are of particular interest in the study of planet formation and evolution. To probe the formation histories of these small planets, it is necessary to derive the planetary masses and radii with precision better than a few percent in order to differentiate their internal compositions in the context of planet evolution models (e.g. Zeng & Sasselov 2013; Brugger et al. 2017). Recent theories have proposed a distinct transition in the composition of small exoplanets (Weiss & Marcy 2014; Rogers 2015). Planets with $R_P \lesssim 1.6\ R_\oplus$ typically have high densities and are predominantly rocky. On the other hand, planets with larger radii typically have lower densities and possess extended H/He envelopes. In fact, planets such as Kepler-10 b (R_P =

1.42 ± 0.03 $R_\oplus$, ρ_P = 8.8 ± 2.5 g cm^{-3}; Batalha et al. 2011),
LHS1140 b (R_P = 1.43 ± 0.10 $R_\oplus$, ρ_P = 12.5 ± 3.4 g cm^{-3};
Dittmann et al. 2017), Kepler-20 b (R_P = 1.87 ± 0.05 $R_\oplus$, ρ_P =
8.2 ± 1.4 g cm^{-3}; Buchhave et al. 2016), and K2-38 b (R_P =
1.55 ± 0.02 $R_\oplus$, ρ_P = 17.5 ± 7.35 g cm^{-3}; Sinukoff et al. 2016)
all have densities higher than that of the Earth ($\rho_\oplus$ = 5.5 g cm^{-3})
and compositions consistent with a rocky world, whereas low
density planets such as GJ 1214 b (R_P = 2.68 ± 0.13 $R_\oplus$, ρ_P =
1.87 ± 0.40 g cm^{-3}; Charbonneau et al. 2009), the Kepler-11
system (R_P = 1.97–4.52 $R_\oplus$, ρ_P = 0.5–3.1 g cm^{-3}; Lissauer
et al. 2011), and HIP 116454 b (R_P = 2.53 ± 0.18 $R_\oplus$, ρ_P =
4.17 ± 1.08 g cm^{-3}; Vanderburg et al. 2015) have solid cores,
and substantial gaseous envelopes.

Recent efforts by the California-*Kepler* Survey (CKS;
Johnson et al. 2017; Fulton et al. 2017) have refined the physi-
cal characteristics of *Kepler* short-period planets ($P < 100$ days)
and their host stars for an in-depth study of the planet size distri-
bution. Their results show a significant lack of planets with sizes
between 1.5 $R_\oplus$ and 2.0 $R_\oplus$. The gap in the radius distribution
can be explained by the "photoevaporation" model (Owen & Wu
2013; Lopez & Fortney 2013), in which the gaseous envelopes
of planets are stripped away as a result of exposure to high inci-
dent flux from their host stars. The CKS also highlighted the
importance of obtaining precise measurements of planet masses
and radii to perform statistically significant studies of the radius
distribution.

In this paper, we report the detection of a 2.37-day tran-
siting super-Earth, K2-265 b. Photometry by *K2* and HARPS
RV measurements were used to constrain the radius and mass
measurements of this planet with a precision of 6 and 13%,
respectively. In Sect. 2, we describe the observations made from
K2, data reduction, and spectroscopic follow-up. Our analyses
and results are presented in Sect. 3, and we conclude the paper
with a summary and discussion in Sect. 4.

2. Observations

2.1. K2 photometry

K2-265 was observed during *K2* Campaign 3 in long cadence
mode. The photometry was obtained between November 2014
and January 2015. The target was independently flagged as a
candidate from two transit searches; the first made use of the
POLAR pipeline (Barros et al. 2016), and the second used the
methods described in Armstrong et al. (2015a,b), where human
input was involved to identify high priority candidates. K2-265
was also independently identified as a planet-hosting candidate
by other search algorithms (Vanderburg et al. 2016; Crossfield
et al. 2016; Mayo et al. 2018).

The *K2* light curve generated from the POLAR pipeline
(Barros et al. 2016) has less white noise than that of Armstrong
et al. (2015a,b), hence the former was used in the planetary
system analysis. The POLAR pipeline is summarised as fol-
lows: the *K2* pixel data was downloaded from the Mikulski
Archive for Space Telescopes (MAST)[1]. The photometric data
was extracted using the adapted CoRoT imagette pipeline from
Barros et al. (2014), which uses an optimal aperture for the pho-
tometric extraction. In this case, the optimal aperture was found
to be close to circular and comprised of 44 pixels. The mod-
ified moment method developed by Stone (1989) was used to
determine the centroid positions for systematic corrections. Flux

---

[1] http://archive.stsci.edu/kepler/data_search/search.php

Table 1. Properties of K2-265 have a nearby bound companion (see text
for detailed description), hence values presented in this table are for the
blended photometry.

Parameter	Value and uncertainty	Source
K2 campaign	3	a
EPIC	206011496	a
2MASS ID	2MASS J22480755−1429407	b
RA(J2000)	22:48:07.56	c
Dec(J2000)	−14:29:40.84	c
μ_{RA} (mas yr^{-1})	30.20 ± 0.09	c
μ_{DEC} (mas yr^{-1})	−23.34 ± 0.06	c
Parallax (mas)	7.18 ± 0.05	c
Photometric magnitudes		
Kp	10.92	a
Gaia G	10.928	c
Johnson *B*	11.845 ± 0.029	d
Johnson *V*	11.102 ± 0.037	d
Sloan *g'*	11.419 ± 0.042	d
Sloan *r'*	10.879 ± 0.047	d
Sloan *i'*	10.689 ± 0.084	d
2-MASS *J*	9.726 ± 0.026	b
2-MASS *H*	9.312 ± 0.022	b
2-MASS *K*s	9.259 ± 0.027	b
WISE W1	9.178 ± 0.022	e
WISE W2	9.213 ± 0.020	e
WISE W3	9.162 ± 0.040	e

Notes. The photometric magnitudes listed were used in deriving the
SED as described in Sect. 3.4. (a) EXOFOP-K2: https://exofop.
ipac.caltech.edu/k2/ (b) Two Micron All Sky Survey (2MASS).
(c) *Gaia* DR2. (d) AAVSO Photometric All-Sky Survey (APASS).
(e) AllWISE.

and position variations of the star on the charge-coupled device
(CCD) can lead to systematics in the data. These were corrected
following the self-flat-fielding method similar to Vanderburg &
Johnson (2014). Figs. 1 and 2 show the final extracted light curve
and the phase-folded light curve of K2-265 respectively. Table 1
gives the photometric properties of K2-265.

2.2. Spectroscopic follow-up

We obtained RV measurements of K2-265 with the HARPS
spectrograph ($R \sim 110\,000$), mounted on the 3.6 m Telescope
at ESO La Silla Observatory (Mayor et al. 2003). A total of
153 observations were made between 2016 October 29 and 2017
November 22 as part of the ESO-K2 large programme[2]. An
exposure time of 1800 s was used for each observation, giv-
ing a signal-to-noise ratio of about 50 per pixel at 5500 Å. The
data were reduced using the HARPS pipeline (Baranne et al.
1996). We computed the RV measurements with the weighted
cross-correlation function (CCF) method using a G2V template
(Baranne et al. 1996; Pepe et al. 2002), and we estimated the
uncertainties in the RVs as described in Bouchy et al. (2001). The
line bisector (BIS), and the full width half maximum (FWHM)
were measured using the methods of Boisse et al. (2011) and
Santerne et al. (2015). Ten observations that were obtained
when the target was close to a bright Moon exhibit a signif-
icant anomaly in their FWHM, up to 500 ms^{-1}. We removed
these data completely from the analyses described in the later

---

[2] Based on observations made with ESO Telescopes at the La Silla
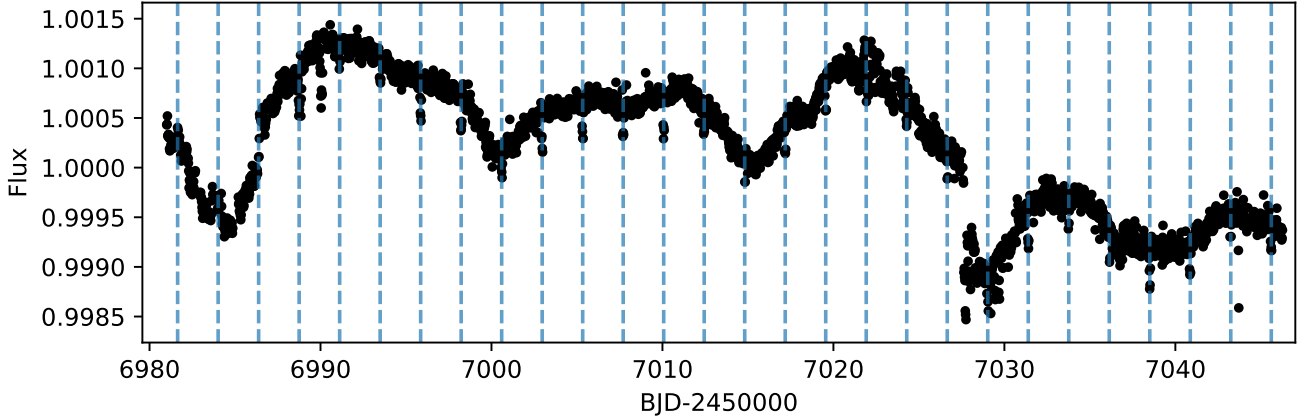Paranal Observatory under programme ID 198.C-0169.

Fig. 1. Detrended *K2* transit light curve of K2-265 with positions of transits marked with blue dashed lines.
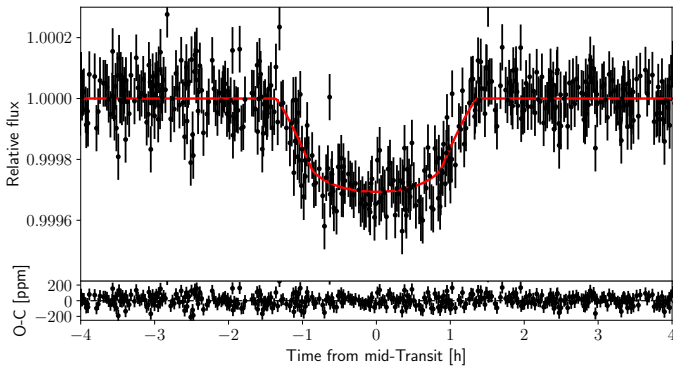

Fig. 2. Phase-folded *K2* light curve of K2-265 is shown in the *top panel* with the ephemeris from our analysis. The best-fit transit model is plotted in a red solid line and the residuals of the fit are plotted in the *bottom panel*.

sections. The remaining 143 RV measurements and their associated uncertainties are reported in Table A.3. The time-series RVs and the phase-folded RVs of K2-265 are shown in Figs. 3 and 4, respectively. Following the calibrations of Noyes et al. (1984), we derived the activity index of $\log R'_{HK} = -4.90 \pm 0.12$. The activity index is used in Sect. 3.3 to derive the stellar rotational period.

2.3. Direct imaging observations

Shallow imaging observations were obtained with the NIRC2 instrument at Keck on 2015-08-04 in the narrow-band Br_γ filter at 2.169 μm (programme N151N2, PI: Ciardi). Several images were acquired with a dithering pattern on-sky and they were simply realigned and median-combined. In the combined image, a candidate companion was clearly detected at close separation from the star. Figure A.1 shows the *K*-bank Keck AO image of K2-265 and the nearby companion, where the contrast of the objects is measured to be Δmag = 8.12 in the *K* band. The relative astrometry of the candidate was estimated using a simple Gaussian fitting on both the star and the candidate. The error on the measurement is conservatively estimated to ~0.5 pixel, i.e. ~5 mas. The relative Keck astrometry was derived following methods described in Vigan et al. (2016) and the following parameters were obtained: $\Delta\alpha = -910 \pm 5$ mas, $\Delta\delta = -363 \pm 5$ mas, separation = 979 ± 5 mas, and position angle = 248.27 ± 0.29 deg.

The target was further observed with the SPHERE instrument on the Very Large Telescope (VLT) instrument in the IRDIFS mode (Vigan et al. 2010; Zurlo et al. 2014). More details on these observations together with the data reduction are presented in Ligi et al. (2018). The relative astrometry of the candidate companion with respect to the star were derived from SPHERE/IRDIFS, and the results are shown in Table A.1. The combined astrometry confirms that the companion is bound with the target star. The SPHERE/IFS data was used to derive a low-resolution near-infrared (NIR) spectrum (Ligi et al. 2018), which we used to characterise the companion star and estimate its contamination in the *K2* photometry (see Sect. 3.2).

2.4. Gaia astrometry

The *Gaia* Data Release 2 (DR2) has surveyed over one billion stars in the Galaxy (Gaia Collaboration 2016, 2018; Lindegren et al. 2018) and provided precise measurements of the parallaxes and proper motions for the sources. K2-265 has a measured parallax of 7.18 ± 0.05 mas, corresponding to a distance of 139 ± 1 pc. The proper motion of K2-265 is $\mu_{RA} = 30.20 \pm 0.09$ mas, $\mu_{Dec} = -23.34 \pm 0.06$ mas. As part of the *Gaia* DR2, the stellar effective temperature of K2-265 was derived from the three photometric bands (Andrae et al. 2018) as $T_{eff} = 5390^{+194}_{-53}$ K. The *G*-band extinction $A_g = 0.101$ and the reddening $E(BP - RP) = 0.065$ estimated from the parallax and magnitudes were used to determine the stellar luminosity, which in turn provides an estimate of the stellar radius as $R_s = 0.914^{+0.02}_{-0.06} R_\odot$ (Andrae et al. 2018). The stellar parameters from the results of *Gaia* DR2 are consistent with the distance estimate, effective temperature, and stellar radius, which are derived in the joint Bayesian analysis in Sect. 3.4. However, *Gaia* DR2 does not detect the companion star in the system and K2-265 is registered as a single object.

3. Analysis and results

3.1. Spectral analysis

The spectral analysis of the host star was performed by co-adding all the individual (Doppler corrected) spectra with IRAF[3]. We first derived the stellar parameters following the analysis of Sousa et al. (2008) by measuring the equivalent

---

[3] IRAF is distributed by National Optical Astronomy Observatories, operated by the Association of Universities for Research in Astronomy, Inc., under contract with the National Science Foundation, USA.
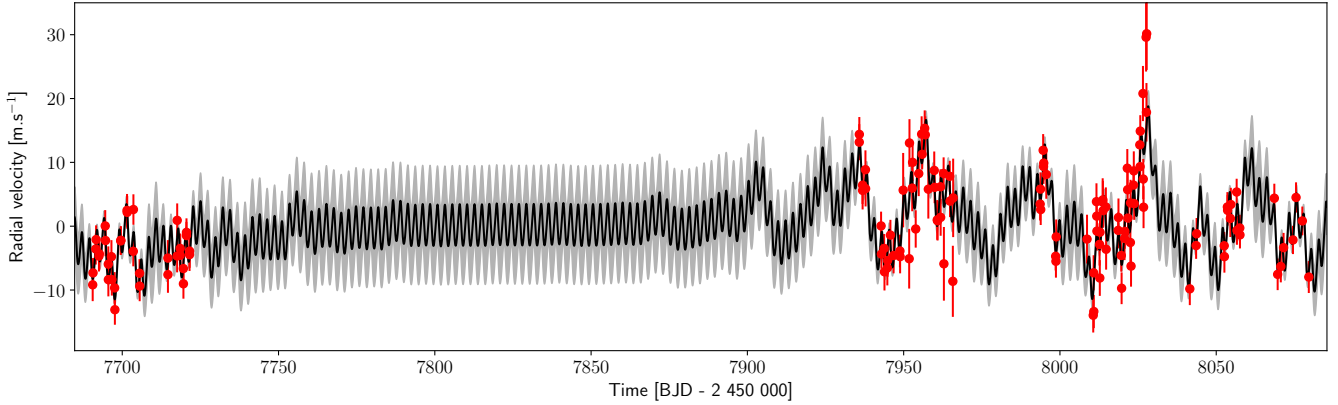
Fig. 3. Time-series HARPS RV measurements (red circles) of K2-265. The best-fit Keplerian orbit of K2-265 b is plotted in black. The stellar activity is fitted with a GP. The grey region show the 1σ confidence interval of the GP.
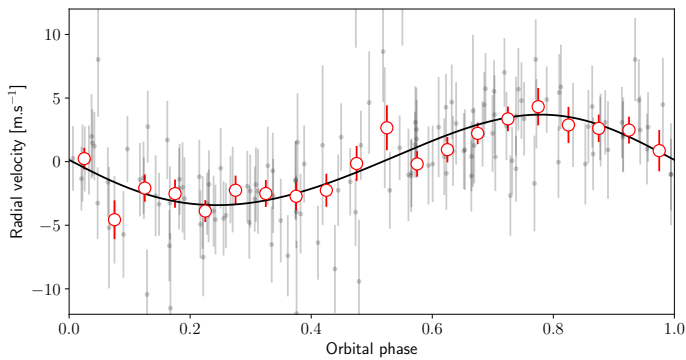

Fig. 4. Phase-folded HARPS RV measurements (black circles) of K2-265 as a function of the orbital phase. The black solid line is the best-fit RV curve. The binned RV measurements are denoted as red open circles.

widths (EW) of Fe I and Fe II lines with version 2 of the ARES code[4] (Sousa et al. 2015). We derived the chemical abundances using the 2014 version of the code MOOG (Sneden 1973), which used the iron excitation and ionisation balance. We obtained the following parameters: $T_{eff} = 5457 \pm 29$ K, $\log g = 4.42 \pm 0.05$ dex, [Fe/H] $= 0.08 \pm 0.02$ dex, microturbulence $\xi_t = 0.81 \pm 0.05$ km s^{-1}. The errors provided in this work for the stellar parameters are precision errors that are intrinsic to the method (Sousa et al. 2011).

The chemical abundances of the host star are found in Table A.2. For more details on this analysis and the complete list of lines are provided in the following works: Adibekyan et al. (2012), Santos et al. (2015), and Delgado Mena et al. (2017). Li and S abundances were derived by spectral synthesis as performed in Delgado Mena et al. (2014) and Ecuvillon et al. (2004), respectively.

3.2. Characterisation of the companion star

To determine the physical parameters of the bound companion, we used the same approach as in Santerne et al. (2016). We fit the magnitude difference between the target and companion star, as observed by SPHERE IRDIFS, with the BT-Settl stellar atmosphere models (Allard et al. 2012). The two stars are

---

[4] The ARES code can be downloaded at `http://www.astro.up.pt/~sousasag/ares/`

bound companions (see Sect. 2.3), hence they have the same distance to Earth and age, and they are assumed to have the same iron abundance. We used a Markov chain Monte Carlo (MCMC) method to derive the companion mass, using the results of the spectral analysis of the target star as priors on the analysis. We used the Dartmouth stellar evolution tracks to convert the companion mass (at a given age and metallicity) into spectroscopic parameters. Our final derivation gives $T_{eff} = 3428 \pm 22$ K, $\log g = 4.870 \pm 0.017$ (cgs), $M_{starB} = 0.40 \pm 0.01$ $M_\odot$, $R_{starB} = 0.391^{+0.006}_{-0.010}$ $R_\odot$, corresponding to a star of spectral type M2 (Cox 2000). Using this result, we integrated the SED models in the Kepler band and derived the contribution of flux contamination in the light curve of star A from star B to be $0.952 \pm 0.024\%$. The derived contamination of the companion star was taken into account in the joint Bayesian analysis in Sect. 3.4 to determine the system parameters of K2-265. The parameters of the companion star and their corresponding uncertainties are reported in Table 2.

3.3. Stellar rotation

Rotational modulation is observed in the detrended *K2* light curve as shown in Fig. 1. We derived the rotational period of K2-265 using multiple methods to determine the origin of the periodic variation.

We first calculated the stellar rotational period with the autocorrelation function (ACF) method as described in McQuillan et al. (2013, 2014) and found the stellar rotational period as 15.14 ± 0.38 d. We observed a further peak at 30.48 ± 0.28 d.

The Lomb–Scargle periodogram (Lomb 1976; Scargle 1982) analysis was performed to determine the periodicity in the RV data. Figure 5 shows the periodogram of the BIS analysis, FWHM, RV measurements, and S index. A clear peak is measured in all four periodograms at 32.2 ± 0.6 d, which is larger than but marginally consistent with the ACF period of 30.48 d at a 2σ level. The timescale of light-curve variation measures the changing visibility of starspots. We attribute the discrepancy between the two rotation periods to latitude variation of the magnetically active regions.

An upper limit of the sky-projected stellar rotational velocity was derived from the FWHM of the HARPS spectra ($v \sin i < 1.9 \pm 0.2$ km s^{-1}). Using the stellar radius in Table 2, we estimate a rotation period $P_{rot} > 26.02 \pm 3.08$ d (assuming an aligned system, $i = 90°$), which agrees with the ~30 d period derived from the photometry and the RV data.

Table 2. System parameters of K2-265 obtained from PASTIS.

Parameter	Value and uncertainty
Stellar parameters	
Star A	
Effective temperature T_{eff} (K)	5477 ± 27
Surface gravity log g (cgs)	4.419 ± 0.053
Iron abundance [Fe/H] (dex)	0.078 ± 0.020
Distance to Earth D (pc)	145 ± 8
Interstellar extinction $E(B-V)$ (mag)	$0.009^{+0.011}_{-0.007}$
Systemic radial velocity γ (km s^{-1})	-18.186 ± 0.002
Stellar density $\rho_\star/\rho_\odot$	0.98 ± 0.19
Stellar mass $M_\star$ ($M_\odot$)	0.915 ± 0.017
Stellar radius $R_\star$ ($R_\odot$)	0.977 ± 0.053
Stellar age τ (Gyr)	9.7 ± 3.0
Star B	
Effective temperature T_{eff} (K)	3428 ± 22
Surface gravity log g (cgs)	4.870 ± 0.017
Stellar mass $M_\star$ ($M_\odot$)	$0.40 \pm 0.0.01$
Stellar radius $R_\star$ ($R_\odot$)	$0.391^{0.006}_{-0.010}$
Planet parameters	
Orbital period P (d)	$2.369172 \pm 8.9 \times 10^{-5}$
Transit epoch T_0 (BJD - 2456000)	$981.6431 \pm 1.6 \times 10^{-3}$
Radial velocity semi-amplitude K (m s^{-1})	3.34 ± 0.43
Orbital inclination i ($^\circ$)	87.7 ± 1.6
Planet-to-star radius ratio k	0.01604 ± 0.00041
Orbital eccentricity e	0.084 ± 0.079
Impact parameter b	0.30 ± 0.20
Transit duration T_{14} (h)	2.266 ± 0.050
Semi-major axis a (AU)	0.03376 ± 0.00021
Planet mass M_p ($M_\oplus$)	6.54 ± 0.84
Planet radius R_p ($R_\oplus$)	1.71 ± 0.11
Planet bulk density ρ_p (g cm^{-3})	7.1 ± 1.8

Notes. Stellar parameters of Star B were derived as described in Sect. 3.2.

Furthermore, the stellar rotation period was also derived following the method of Mamajek & Hillenbrand (2008). In summary, we used the B − V colour from APASS to find the convective turnover time τ_c using calibrations from Noyes et al. (1984). We then used the measured Mount Wilson index $S_{MW} = 0.195 \pm 0.025$ to derive log $R'_{HK} = -4.90 \pm 0.12$, from which we determine the Rossby number $R_o = 1.94$ using calibrations from Mamajek & Hillenbrand (2008). Finally, using the relation $P_{rot} = R_o \times \tau_c$, we calculate the stellar rotation period as 32 ± 10 d.

3.4. Joint Bayesian analysis with PASTIS

We employed a Bayesian approach to derive the physical parameters of the host star and the planet. We jointly analysed the *K2* photometric light curve, the HARPS RV measurements and the spectral energy distribution (SED) observed by the APASS[5], 2MASS, and the Wide-field Infrared Survey Explorer (WISE) surveys (Munari et al. 2014; Cutri 2014; a full list of host star magnitudes can be found in Table 1) using the PASTIS software (Díaz et al. 2014; Santerne et al. 2015). The light curve was modelled using the jktebop package (Southworth 2008) by taking an oversampling factor of 30 to account for the long integration

---

[5] https://www.aavso.org/apass

time of the *K2* data (Kipping 2010). The RVs were modelled with Keplerian orbits. Following similar approaches to Barros et al. (2017) and Santerne et al. (2018), we used a Gaussian process (GP) regression to model the activity signal of the star. We modelled the SED using the BT-Settl library of stellar atmosphere models (Allard et al. 2012).

We derived the system parameters via the MCMC method. The spectroscopic parameters of K2-265A were converted into physical stellar parameters using the Dartmouth evolution tracks (Dotter et al. 2008) at each step of the chain. The quadratic limb darkening coefficients were also computed using the stellar parameters and tables of Claret & Bloemen (2011).

For the stellar parameters, we used normal distribution priors centred on the values derived in our spectral analysis. We chose a normal prior for the orbital ephemeris centred on values found by the detection pipeline. Furthermore, we adopted a sine distribution for the inclination of the planet. Uninformative priors were used for the other parameters. The priors of the fitted parameters used in the model can be found in Table A.4.

Twenty MCMC chains of 3×10^5 iterations were run during the MCMC analysis, where the starting points were randomly drawn from the joint prior. The Kolmogorov–Smirnov test was used to test for convergence in each chain. We then removed the burn-in phase and merged the converged chains to derive the system parameters.

3.5. Stellar age

From the joint analysis of the observational data, together with the Dartmouth stellar evolution tracks, the age of K2-265 was determined as $\tau_{iso} = 9.7 \pm 3.0$ Gyr. The stellar rotation analysis in Sect. 3.3 found that K2-265 has a rotation period of ∼30 d. We adopted a rotational period of 32.2 ± 0.6 d and followed the methods by Barnes (2010) to find that K2-265 has a gyrochronological age of $\tau_{gyro} = 5.34 \pm 0.19$ Gyr. We further derived the age of K2-265 using the relation between the [Y/Mg] abundance ratio and stellar age (Nissen 2015; Tucci Maia et al. 2016) and found an age of $\tau_{[Y/Mg]} = 3.97 \pm 2.59$ Gyr. The value $\tau_{[Y/Mg]}$ agrees with τ_{gyro} within 1σ uncertainty but is lower than the derived isochronal age. The low lithium abundance A(Li II) < 0.45 of the host star obtained from spectral analysis (Sect. 3.1) suggests that the host is not young. Hence, it is likely that the host is of at least an intermediate age.

4. Discussion and conclusions

K2-265 b has a mass of 6.54 ± 0.84 $M_\oplus$ and radius of 1.71 ± 0.11 $R_\oplus$ (Fig. 6). This corresponds to a bulk density of 7.1 ± 1.8 g cm^{-3}, which is slightly higher than that of the density of the Earth. We applied a number of theoretical models to investigate the interior composition of the planet.

Fortney et al. (2007) modelled the radii of planets with a range of different masses at various compositions and derived an analytical function that allows an estimate of the rock mass fraction (rmf) of ice-rock-iron planets. We find a rmf of 0.84 for K2-265 b, which is equivalent to a rock-to-iron ratio of 0.84/0.16, i.e. a rock fraction that is higher than the Earth. Seager et al. (2007) also used interior models of planets to study the mass–radius relation of solid planets. By assuming the planets are composed primarily of iron, silicates, water, and carbon compounds, Seager et al. (2007) showed that masses and radii of terrestrial planets follow a power law. Using the derived best-fit mass and radius of K2-265 b, the bulk composition of the planet
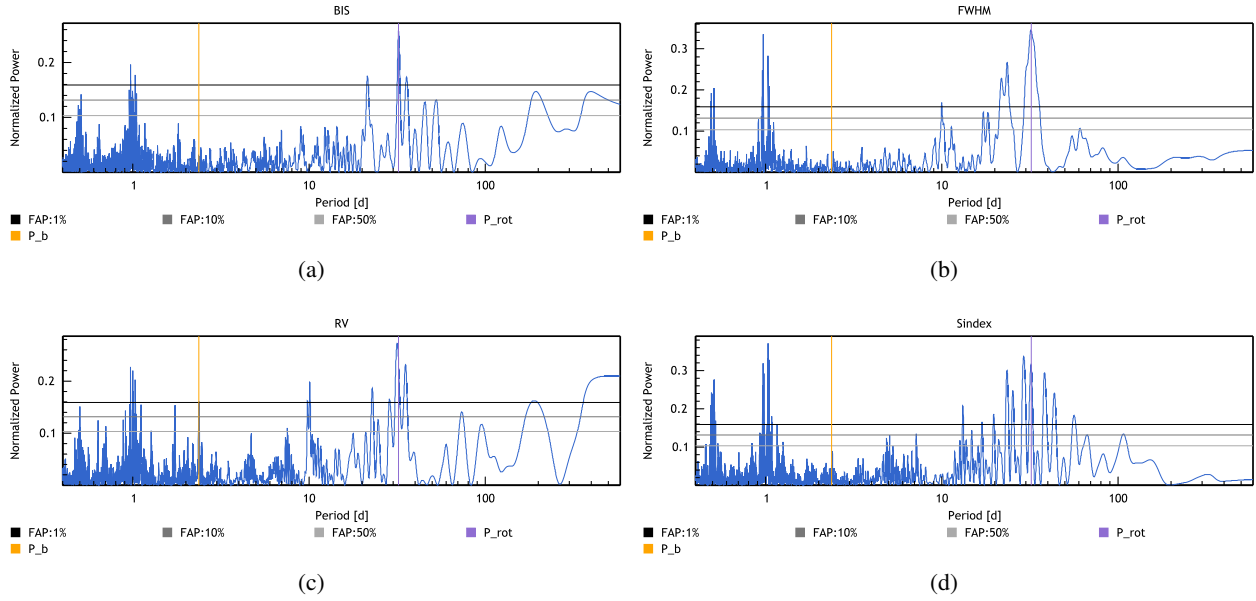
(a)

(b)

(c)

(d)

Fig. 5. Lomb–Scargle periodogram of (*panel a*) BIS span; (*panel b*) FWHM; (*panel c*) RV; (*panel d*) S index (S_{MW}). The peak position is indicated by the purple line and corresponds to a period of 32.2 ± 0.6 d. The orbital period of K2-265 b is indicated by the yellow line, and the planet signal is only significant in the RV at the 1% FAP level.
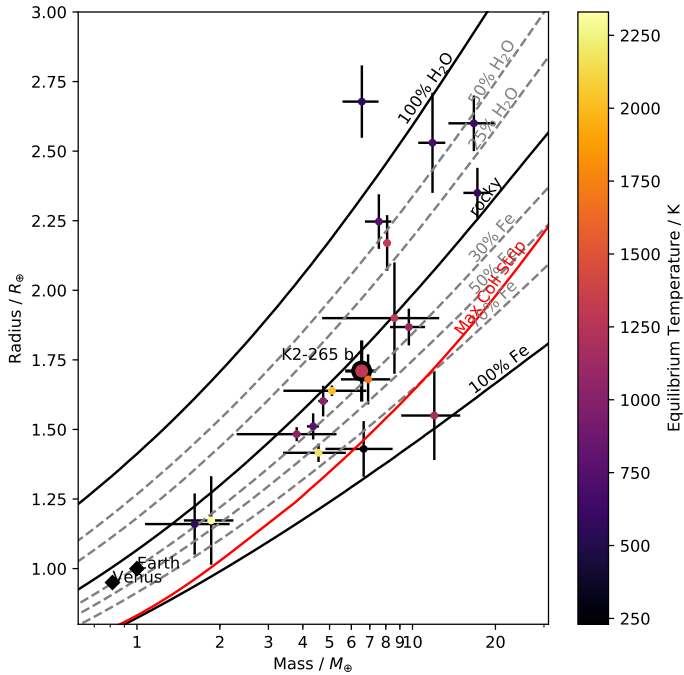

Fig. 6. Mass–radius diagram of confirmed Earth-sized planets with masses up to 20 $M_\oplus$. Data were taken from NASA Exoplanet archive[6]. The mass–radius relations were taken from Zeng et al. (2016). From top to bottom: black solid lines denotes a pure water, pure rock, and pure iron composition. The grey dashed lines between the solid lines represent mass–radius relations for water-rock and rock-iron composites. The red solid line indicates the lower limit of a planet radius as a result of collisional stripping (Marcus et al. 2010). K2-265 b has a composition consistent with a rocky terrestrial planet.

was determined to be predominantly rocky with >70% of silicate mantle by mass.

We performed a more detailed investigation of the composition of K2-265 b using the interior model of Brugger et al. (2017). This model considers planets composed of three differentiated layers: core (metals), mantle (rocks), and a liquid water envelope. Figure 7 shows the possible compositions of K2-265 b inferred from the 1σ uncertainties on the mass and radius of the planet. By focussing on terrestrial compositions only (i.e. without any water), we show that the central mass and radius of the planet are best fitted with a rock mass fraction of 81%, which is consistent with other theoretical predictions. However, given the uncertainties on the fundamental parameters, the rmf remains poorly constrained, namely, within the 44–100% range. If we assume that the stellar Fe/Si ratio (here 0.90 ± 0.41) can be used as a proxy for the bulk planetary value (Dorn et al. 2015; Brugger et al. 2017), this range is reduced to 60–83%. In the case of a water-rich K2-265 b, the model only allows us to derive an upper limit on the water mass fraction (wmf) of the planet. Indeed, given the high equilibrium temperature of the planet (∼1300 K assuming an Earth-like albedo), water would be in the gaseous and supercritical phases, which are less dense than the liquid phase. From the uncertainties on the mass, radius, and bulk Fe/Si ratio of K2-265 b, we infer that this planet cannot present a wmf larger than 31%.

The CKS measured precise stellar parameters of Kepler host stars using spectroscopic follow-up (Johnson et al. 2017) and refined the planetary radii to study the planet size distribution and planet occurrence rate (Fulton et al. 2017). The survey has revealed a bimodal distribution of small planet sizes. Planets tend to have radii of either ≈1.3 $R_\oplus$ or ≈2.4 $R_\oplus$, with a deficit of planets at ≈ 1.8 $R_\oplus$. The survey confirms the prediction by Owen & Wu (2013), whereby a gap in the planetary radius distribution exists as a consequence of atmospheric erosion by the photo-evaporation mechanism. Alternatively, the core-powered mass loss mechanism could also drive the evaporation of small planets (Ginzburg et al. 2016, 2018).

Because of its close proximity to the host star, the super-Earth K2-265 b is exposed to strong stellar irradiation. The gas envelope of the planet could be evaporated as a result. This
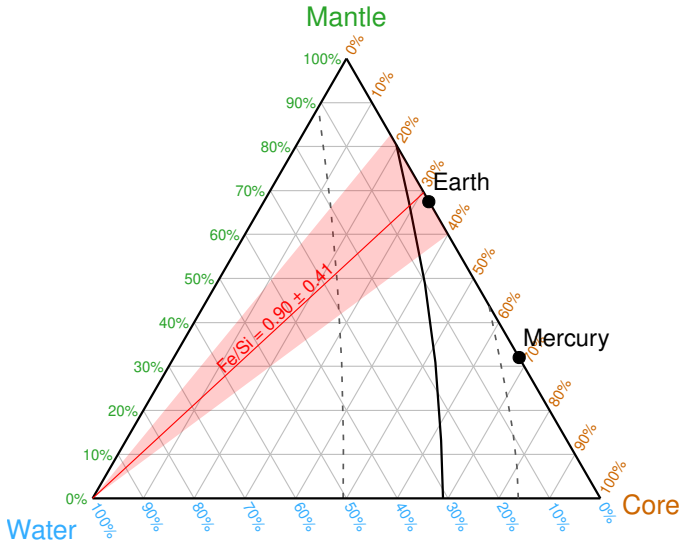
---

[6] https://exoplanetarchive.ipac.caltech.edu/index.html

Fig. 7. Ternary diagram showing the possible composition of K2-265 b. The thick black line indicates the allowed composition of the planet inferred from the central values of the mass and radius of the planet, and the dashed lines denote the deviations from this line allowed by the 1σ uncertainties on the fundamental parameters. The red line and area show the compositions compatible with the planetary bulk Fe/Si ratio derived for K2-265 b from the stellar value. Compositions of the Earth and Mercury are shown for reference.
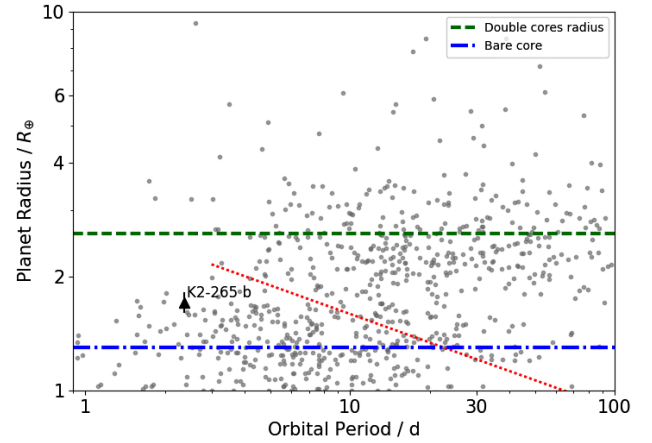

Fig. 8. Planet radius distribution as a function of orbital period. The grey circles denote the planet sample obtained from the CKS sample (Fulton et al. 2017). The blue dot-dashed line and the green dashed line indicate the peak of the bimodal distribution of the planet radius distribution, where planets tend to favour radii of ∼1.3 $R_\oplus$ and ∼2.4 $R_\oplus$ due to the photoevaporation mechanism. The red dotted line indicates the lower limit of the photoevaporation valley derived from Owen & Wu (2017).

process was observed in a number of systems (e.g. HD209458 b; Vidal-Madjar et al. 2003, GJ 436 b; Ehrenreich et al. 2015). The present irradiance of the planet is $S = S_\oplus (L_s/L_\odot)(\mathrm{AU}/a)^2 = 9.32 \times 10^5$ Wm^{-2}, where L_s and $L_\odot$ are the luminosity of the star and the Sun, $S_\oplus$ is the solar irradiance on Earth, and a is the semi-major axis of the planet. The equilibrium temperature of the K2-265 b can be estimated using Eq. (1) of López-Morales & Seager (2007): $T_{eq} = T_{eff}(R_s/a)^{1/2}[f(1-A_B)]$, where f and A_B are the reradiation factor and the Bond albedo of the planet. Assuming an Earth-like Bond albedo $A_B = 0.3$ and that the incident radiation is redistributed around the atmosphere (i.e. $f = 1/4$), the equilibrium temperature of K2-265 b is $T_{eff} \approx 1300$ K.

Indeed, K2-265 b lies below the lower limit of the photoevaporation valley as shown in the 2D radius distribution plot in Fig. 8. This implies that the planet could have been stripped bare from photoevaporation, revealing its naked core. This atmospheric stripping process is presumed to have occurred in the first ≈100 Myr since the birth of the planet when X-ray emission is saturated (Jackson et al. 2012), after which the X-ray emission decays. We estimated the total X-ray luminosity of K2-265 over its lifetime, E_x^{tot}, using the X-ray-age relation of Jackson et al. (2012). Using the results of Sect. 3.5, we adopted a mean age of 6.32 Gyr for the host star. The X-ray-to-bolometric luminosity ratio in the saturated regime for a $B - V = 0.743$ star is $\log(L_x/L_{bol}) = -3.71 \pm 0.05 \pm 0.47$. The corresponding turn-off age is $\log\tau_{sat} = 8.03 \pm 0.06 \pm 0.31$, where the decrease in X-ray emission follows a power law ($\alpha = 1.28 \pm 0.17$). Over the lifetime of the star, $E_x^{tot} = 6.70 \times 10^{45}$ ergs (assuming efficiency factor $\eta = 0.25$) and K2-265 b is expected to have lost 2.7% of its mass under the constant-density assumption. K2-265 b has a predominantly rocky interior as shown in Fig. 7. This indicates that the planet was likely formed inside the ice line and could have either migrated to its current orbital separation well before ≈100 Myr or accreted its mass locally (Owen & Wu 2017).

K2-265 b is among the denser super-Earths below the photoevaporation gap. In addition to photoevaporation, giant impact between super-Earths could drive mass loss in the planetary atmosphere. Super-Earths are thought to have formed via accretion in gas discs, followed by migration and eccentricity damping due to their interactions with the gas disc (e.g. Lee & Chiang 2015), leading to densely packed planetary systems. As the gas disc disperses, secular perturbation between planets excites their eccentricity, triggering giant impacts between the bodies before the system becomes stable (Cossou et al. 2014). Two planets of comparable sizes could collide at a velocity beyond the surface escape velocity (Agnor & Asphaug 2004; Marcus et al. 2009). The impact could lead to a reduction in the planet envelope-to-core-mass ratio, hence an increase in the mean density and alteration of the bulk composition of the planet (Liu et al. 2015; Inamdar & Schlichting 2016).

Discoveries of super-Earths have shown a diversity of small planets in the mass–radius diagram. Precise RV and photometric measurements with an accuracy of a few percent are necessary to put strong constraints on the planetary mass and radius and provide a precise bulk composition. The core composition of the planet can be derived as a result. In particular, the mass fraction of a planetary core can inform us of the formation and evolution history of the planet. K2-265 b has a precisely determined mass (13%) and radius (6%) and the composition of the planet is consistent with a rocky planet. Its small radius and short orbital period suggest that K2-265 b could have been photoevaporated to a bare rocky core. Its high rock-to-mass fraction implies a planet formation within the ice line. Studying planets with an exposed core could provide valuable insight to planet formation via the core accretion mechanism. The increasing sample of small planets will help distinguish planet origins, identify types of mass loss mechanism, and probe the efficiency of atmospheric evaporation processes.

References

Adibekyan, V. Z., Sousa, S. G., Santos, N. C., et al. 2012, A&A, 545, A32
Agnor, C., & Asphaug, E. 2004, ApJ, 613, L157
Allard, F., Homeier, D., & Freytag, B. 2012, Phil. Trans. R. Soc. London, Ser. A, 370, 2765
Andrae, R., Fouesneau, M., Creevey, O., et al. 2018, A&A, 616, A8
Armstrong, D. J., Kirk, J., Lam, K. W. F., et al. 2015a, A&A, 579, A19
Armstrong, D. J., Santerne, A., Veras, D., et al. 2015b, A&A, 582, A33
Baranne, A., Queloz, D., Mayor, M., et al. 1996, A&AS, 119, 373
Barnes, S. A. 2010, ApJ, 722, 222
Barros, S. C. C., Almenara, J. M., Deleuil, M., et al. 2014, A&A, 569, A74
Barros, S. C. C., Almenara, J. M., Demangeon, O., et al. 2015, MNRAS, 454, 4267
Barros, S. C. C., Demangeon, O., & Deleuil, M. 2016, A&A, 594, A100
Barros, S. C. C., Gosselin, H., Lillo-Box, J., et al. 2017, A&A, 608, A25
Batalha, N. M. 2014, Proc. Natl. Acad. Sci., 111, 12647
Batalha, N. M., Borucki, W. J., Bryson, S. T., et al. 2011, ApJ, 729, 27
Batalha, N. M., Rowe, J. F., Bryson, S. T., et al. 2013, ApJS, 204, 24
Boisse, I., Bouchy, F., Hébrard, G., et al. 2011, A&A, 528, A4
Bonfils, X., Delfosse, X., Udry, S., et al. 2013, A&A, 549, A109
Borucki, W. J., Koch, D., Basri, G., et al. 2010, Science, 327, 977
Borucki, W. J., Koch, D. G., Basri, G., et al. 2011, ApJ, 736, 19
Bouchy, F., Pepe, F., & Queloz, D. 2001, A&A, 374, 733
Brugger, B., Mousis, O., Deleuil, M., & Deschamps, F. 2017, ApJ, 850, 93
Buchhave, L. A., Dressing, C. D., Dumusque, X., et al. 2016, AJ, 152, 160
Charbonneau, D., Berta, Z. K., Irwin, J., et al. 2009, Nature, 462, 891
Claret, A., & Bloemen, S. 2011, A&A, 529, A75
Cossou, C., Raymond, S. N., Hersant, F., & Pierens, A. 2014, A&A, 569, A56
Cox, A. N. 2000, Astrophysical Quantities (New York: Springer)
Crossfield, I. J. M., Ciardi, D. R., Petigura, E. A., et al. 2016, ApJS, 226, 7
Cutri, R. M. e. 2014, VizieR Online Data Catalog: II/328
Delgado Mena, E., Israelian, G., González Hernández, J. I., et al. 2014, A&A, 562, A92
Delgado Mena, E., Tsantaki, M., Adibekyan, V. Z., et al. 2017, A&A, 606, A94
Díaz, R. F., Almenara, J. M., Santerne, A., et al. 2014, MNRAS, 441, 983
Dittmann, J. A., Irwin, J. M., Charbonneau, D., et al. 2017, Nature, 544, 333
Dorn, C., Khan, A., Heng, K., et al. 2015, A&A, 577, A83
Dotter, A., Chaboyer, B., Jevremović, D., et al. 2008, ApJS, 178, 89
Dressing, C. D., & Charbonneau, D. 2013, ApJ, 767, 95
Ecuvillon, A., Israelian, G., Santos, N. C., et al. 2004, A&A, 426, 619
Ehrenreich, D., Bourrier, V., Wheatley, P. J., et al. 2015, Nature, 522, 459
Fortney, J. J., Marley, M. S., & Barnes, J. W. 2007, ApJ, 659, 1661
Fulton, B. J., Petigura, E. A., Howard, A. W., et al. 2017, AJ, 154, 109
Gaia Collaboration (Prusti, T., et al.) 2016, A&A, 595, A1
Gaia Collaboration (Brown, A. G. A., et al.) 2018, A&A, 616, A1
Ginzburg, S., Schlichting, H. E., & Sari, R. 2016, ApJ, 825, 29
Ginzburg, S., Schlichting, H. E., & Sari, R. 2018, MNRAS, 476, 759
Howard, A. W., Marcy, G. W., Bryson, S. T., et al. 2012, ApJS, 201, 15
Howell, S. B., Sobeck, C., Haas, M., et al. 2014, PASP, 126, 398
Inamdar, N. K., & Schlichting, H. E. 2016, ApJ, 817, L13
Jackson, A. P., Davis, T. A., & Wheatley, P. J. 2012, MNRAS, 422, 2024
Johnson, J. A., Petigura, E. A., Fulton, B. J., et al. 2017, AJ, 154, 108
Kipping, D. M. 2010, MNRAS, 408, 1758
Koch, D. G., Borucki, W. J., Basri, G., et al. 2010, ApJ, 713, L79
Lee, E. J., & Chiang, E. 2015, ApJ, 811, 41
Ligi, R., Demangeon, O., Barros, S., et al. 2018, AJ, 156, 182
Lindegren, L., Hernandez, J., Bombrun, A., et al. 2018, A&A, 616, A2
Lissauer, J. J., Fabrycky, D. C., Ford, E. B., et al. 2011, Nature, 470, 53
Liu, S.-F., Hori, Y., Lin, D. N. C., & Asphaug, E. 2015, ApJ, 812, 164
Lomb, N. R. 1976, Ap&SS, 39, 447
Lopez, E. D., & Fortney, J. J. 2013, ApJ, 776, 2
López-Morales, M., & Seager, S. 2007, ApJ, 667, L191
Mamajek, E. E., & Hillenbrand, L. A. 2008, ApJ, 687, 1264
Marcus, R. A., Stewart, S. T., Sasselov, D., & Hernquist, L. 2009, ApJ, 700, L118
Marcus, R. A., Sasselov, D., Hernquist, L., & Stewart, S. T. 2010, ApJ, 712, L73
Mayo, A. W., Vanderburg, A., Latham, D. W., et al. 2018, AJ, 155, 136
Mayor, M., Pepe, F., Queloz, D., et al. 2003, The Messenger, 114, 20
Mayor, M., Marmier, M., Lovis, C., et al. 2011, ArXiv e-prints [arXiv:1109.2497]
McQuillan, A., Mazeh, T., & Aigrain, S. 2013, ApJ, 775, L11
McQuillan, A., Mazeh, T., & Aigrain, S. 2014, ApJS, 211, 24
Montet, B. T., Morton, T. D., Foreman-Mackey, D., et al. 2015, ApJ, 809, 25
Munari, U., Henden, A., Frigo, A., et al. 2014, AJ, 148, 81
Nissen, P. E. 2015, A&A, 579, A52
Noyes, R. W., Weiss, N. O., & Vaughan, A. H. 1984, ApJ, 287, 769
Owen, J. E., & Wu, Y. 2013, ApJ, 775, 105
Owen, J. E., & Wu, Y. 2017, ApJ, 847, 29
Pepe, F., Mayor, M., Rupprecht, G., et al. 2002, The Messenger, 110, 9
Petigura, E. A., Howard, A. W., & Marcy, G. W. 2013, Proc. Natl. Acad. Sci., 110, 19273
Pope, B. J. S., Parviainen, H., & Aigrain, S. 2016, MNRAS, 461, 3399
Rogers, L. A. 2015, ApJ, 801, 41
Santerne, A., Díaz, R. F., Almenara, J.-M., et al. 2015, MNRAS, 451, 2337
Santerne, A., Hébrard, G., Lillo-Box, J., et al. 2016, ApJ, 824, 55
Santerne, A., Brugger, B., Armstrong, D. J., et al. 2018, Nat. Astron., 2, 393
Santos, N. C., Adibekyan, V., Mordasini, C., et al. 2015, A&A, 580, L13
Scargle, J. D. 1982, ApJ, 263, 835
Seager, S., Kuchner, M., Hier-Majumder, C. A., & Militzer, B. 2007, ApJ, 669, 1279
Sinukoff, E., Howard, A. W., Petigura, E. A., et al. 2016, ApJ, 827, 78
Sneden, C. A. 1973, Ph.D. Thesis, The University of Texas at Austin, Texas
Sousa, S. G., Santos, N. C., Mayor, M., et al. 2008, A&A, 487, 373
Sousa, S. G., Santos, N. C., Israelian, G., et al. 2011, A&A, 526, A99
Sousa, S. G., Santos, N. C., Adibekyan, V., Delgado-Mena, E., & Israelian, G. 2015, A&A, 577, A67
Southworth, J. 2008, MNRAS, 386, 1644
Stone, R. C. 1989, AJ, 97, 1227
Tucci Maia, M., Ramírez, I., Meléndez, J., et al. 2016, A&A, 590, A32
Vanderburg, A., & Johnson, J. A. 2014, PASP, 126, 948
Vanderburg, A., Montet, B. T., Johnson, J. A., et al. 2015, ApJ, 800, 59
Vanderburg, A., Latham, D. W., Buchhave, L. A., et al. 2016, ApJS, 222, 14
Vidal-Madjar, A., Lecavelier des Etangs, A., Désert, J.-M., et al. 2003, Nature, 422, 143
Vigan, A., Moutou, C., Langlois, M., et al. 2010, MNRAS, 407, 71
Vigan, A., Bonnefoy, M., Ginski, C., et al. 2016, A&A, 587, A55
Weiss, L. M., & Marcy, G. W. 2014, ApJ, 783, L6
Zeng, L., & Sasselov, D. 2013, PASP, 125, 227
Zeng, L., Sasselov, D. D., & Jacobsen, S. B. 2016, ApJ, 819, 127
Zurlo, A., Vigan, A., Mesa, D., et al. 2014, A&A, 572, A85

Appendix A: Supplementary tables and figures

Table A.1. NIRC2 and IRDIS astrometry of the candidate companion.

Instrument	Date	$\Delta\alpha$ (mas)	$\Delta\delta$ (mas)	Sep. (mas)	Pos. ang. (deg)
Keck/NIRC2	2015-08-04	-910 ± 5	-363 ± 5	979 ± 5	248.27 ± 0.29
VLT/SPHERE	2015-08-04	-906 ± 1	-368 ± 1	978 ± 1	247.87 ± 0.20
VLT/SPHERE	2017-08-30	-903 ± 1	-365 ± 1	975 ± 1	247.99 ± 0.01

Table A.2. Chemical abundances of the host star, relative to the Sun.

| Element (X/H)	Abundance (dex)	Number of lines
C 1	0.01 ± 0.05	2
O 1	0.14 ± 0.10	2
Na 1	0.059 ± 0.023	2
Mg 1	0.068 ± 0.068	3
Al 1	0.012 ± 0.023	2
Si 1	0.053 ± 0.037	11
S 1	0.05 ± 0.08	2
Ca 1	0.102 ± 0.051	9
Sc 1	0.081 ± 0.053	3
Sc 2	0.099 ± 0.026	6
Ti 1	0.117 ± 0.045	18
Ti 2	0.064 ± 0.034	5
V 1	0.186 ± 0.052	6
Cr 1	0.088 ± 0.036	17
Mn 1	0.128 ± 0.049	5
Co 1	0.130 ± 0.04	7
Ni 1	0.069 ± 0.023	40
Cu 1	0.10 ± 0.04	4
Zn 1	0.00 ± 0.02	3
Sr 1	0.17 ± 0.08	1
Y 2	0.09 ± 0.04	6
Zr 2	0.13 ± 0.04	4
Ba 2	0.07 ± 0.04	3
Ce 2	0.13 ± 0.07	4
Nd 2	0.11 ± 0.03	2
A(Li 1)[a]	<0.45	1

Notes. [a] $A(Li) = \log[N(Li)/N(H)] + 12$.
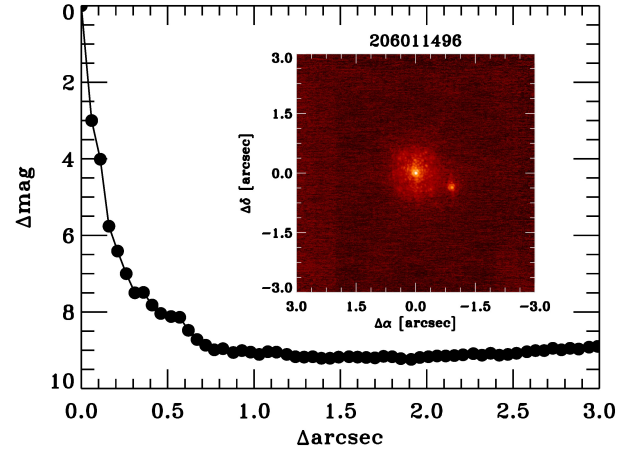
Fig. A.1. K-band Keck AO image shows a companion at a separation of = 979 ± 5 mas.

Table A.3. Radial velocity data.

Time (BJD)	RV (km s^{-1})	σRV (m s^{-1})	*FWHM* (km s^{-1})	σ*FWHM* (m s^{-1})	BIS (m s^{-1})	σBIS (m s^{-1})	S_{MW}	σS_{MW}	S/N
57690.54527	−18.19493	2.01	6.9428	4.0	−27.1	4.0	0.1820	0.0064	46.8
57690.65420	−18.19306	1.70	6.9393	3.4	−24.5	3.4	0.1826	0.0056	57.3
57691.52542	−18.18932	1.84	6.9423	3.7	−27.3	3.7	0.1755	0.0056	51.0
57691.64089	−18.18784	1.57	6.9380	3.1	−19.0	3.1	0.1789	0.0052	62.8
57692.54337	−18.19043	1.82	6.9336	3.6	−17.0	3.6	0.1799	0.0057	52.2
57692.66890	−18.19007	2.03	6.9400	4.1	−18.4	4.1	0.1868	0.0082	48.1
57694.55555	−18.18570	1.90	6.9404	3.8	−30.9	3.8	0.1873	0.0061	50.0
57694.65367	−18.18799	1.89	6.9472	3.8	−17.4	3.8	0.1825	0.0071	51.6
57695.53842	−18.19169	2.29	6.9375	4.6	−34.0	4.6	0.1877	0.0077	40.8
57695.55993	−18.19412	2.09	6.9479	4.2	−24.2	4.2	0.1730	0.0065	44.5
57696.54203	−18.19052	2.05	6.9560	4.1	−26.0	4.1	0.1857	0.0068	45.8
57696.67629	−18.19411	1.94	6.9507	3.9	−22.7	3.9	0.1817	0.0075	50.1
57697.56269	−18.19541	1.90	6.9536	3.8	−29.4	3.8	0.1788	0.0061	49.7
57697.64405	−18.19883	1.74	6.9470	3.5	−26.9	3.5	0.1855	0.0058	55.5
57699.51415	−18.18805	1.53	6.9476	3.1	−24.6	3.1	0.2188	0.0041	62.7
57699.56041	−18.18795	1.56	6.9584	3.1	−18.3	3.1	0.2205	0.0048	62.6
57701.53183	−18.18327	2.03	6.9532	4.1	−26.0	4.1	0.2197	0.0061	45.9
57701.57985	−18.18358	2.01	6.9494	4.0	−26.0	4.0	0.2343	0.0061	46.5
57703.53660	−18.18968	1.74	6.9375	3.5	−15.2	3.5	0.2164	0.0054	55.2
57703.57238	−18.18313	1.78	6.9565	3.6	−15.9	3.6	0.2190	0.0055	53.8
57705.53138	−18.19312	1.53	6.9390	3.1	−12.6	3.1	0.2031	0.0045	64.9
57705.57766	−18.19513	1.76	6.9337	3.5	−16.9	3.5	0.2142	0.0060	55.6
57714.60057	−18.19074	2.33	6.9600	4.7	−13.1	4.7	0.2277	0.0086	41.2
57714.62010	−18.19333	2.37	6.9489	4.7	−12.6	4.7	0.2225	0.0099	41.4
57717.55993	−18.19042	2.01	6.9418	4.0	−17.8	4.0	0.1746	0.0073	48.1
57717.58112	−18.18483	2.13	6.9487	4.3	−17.2	4.3	0.1940	0.0079	45.2
57718.53008	−18.19030	1.78	6.9488	3.6	−17.7	3.6	0.1990	0.0061	54.1
57718.55149	−18.18923	1.73	6.9507	3.5	−12.9	3.5	0.2019	0.0060	56.2
57719.55290	−18.19238	1.71	6.9511	3.4	−22.8	3.4	0.1884	0.0056	56.5
57719.57368	−18.19477	1.71	6.9425	3.4	−18.4	3.4	0.1994	0.0057	56.7
57720.53108	−18.18721	1.45	6.9469	2.9	−14.2	2.9	0.1922	0.0046	70.4
57720.55102	−18.18671	1.52	6.9397	3.0	−17.1	3.0	0.1968	0.0051	65.7
57721.53077	−18.19020	2.01	6.9556	4.0	−24.1	4.0	0.1938	0.0070	47.5
57721.55300	−18.18965	2.09	6.9408	4.2	−14.9	4.2	0.1838	0.0076	45.7
57935.79544	−18.17258	2.34	6.9898	4.7	−7.0	4.7	0.2700	0.0091	42.0
57935.81684	−18.17136	2.21	6.9761	4.4	−5.1	4.4	0.2564	0.0084	44.2
57936.84590	−18.17932	2.48	6.9803	5.0	−15.5	5.0	0.2820	0.0100	39.7
57936.86711	−18.18014	2.53	6.9722	5.1	1.8	5.1	0.2668	0.0104	39.1
57937.77515	−18.17689	2.58	6.9604	5.2	−6.9	5.2	0.2415	0.0105	38.3
57937.82206	−18.17986	2.30	6.9765	4.6	−15.1	4.6	0.2444	0.0088	42.4
57942.77873	−18.18570	1.58	6.9310	3.2	−19.1	3.2	0.2124	0.0046	61.4
57942.88776	−18.19012	1.65	6.9373	3.3	−15.1	3.3	0.2270	0.0066	61.1
57943.75116	−18.18923	1.62	6.9337	3.2	−13.2	3.2	0.1961	0.0048	60.4
57943.86160	−18.19289	2.46	6.9371	4.9	−21.2	4.9	0.1863	0.0097	39.7
57944.77832	−18.19228	2.24	6.9244	4.5	−15.5	4.5	0.1864	0.0082	42.9
57944.86188	−18.19112	1.99	6.9344	4.0	−25.0	4.0	0.1829	0.0075	48.7
57945.75844	−18.18714	1.79	6.9247	3.6	−23.8	3.6	0.1759	0.0057	53.7
57946.77897	−18.19034	2.30	6.9292	4.6	−25.4	4.6	0.1791	0.0080	42.0
57948.80722	−18.18963	2.00	6.9241	4.0	−25.8	4.0	0.1690	0.0069	48.4
57948.86573	−18.19051	2.09	6.9274	4.2	−21.6	4.2	0.1760	0.0080	46.5
57949.84184	−18.18010	5.61	6.9040	11.2	−11.5	11.2	0.1322	0.0280	20.3
57951.76491	−18.19084	4.40	6.9380	8.8	−23.9	8.8	0.2072	0.0226	24.4
57951.85922	−18.17271	3.38	6.9374	6.8	−17.4	6.8	0.1802	0.0169	30.3
57952.73957	−18.17978	3.26	6.9507	6.5	−13.5	6.5	0.1720	0.0148	31.2
57952.86046	−18.17574	2.49	6.9466	5.0	−27.4	5.0	0.1881	0.0111	39.7
57953.85555	−18.18618	2.46	6.9581	4.9	−19.0	4.9	0.1945	0.0105	40.1
57954.82099	−18.17750	3.16	6.9479	6.3	−23.7	6.3	0.1541	0.0150	32.5

Notes. The Barycentric Julian Date (BJD) is given with an offset of 2400000. Signal-to-noise ratio (S/N) is given per CCD pixel at 550 nm.

Table A.3. continued.

Time (BJD)	RV (km s^{-1})	σRV (m s^{-1})	*FWHM* (km s^{-1})	σ*FWHM* (m s^{-1})	BIS (m s^{-1})	σBIS (m s^{-1})	S_{MW}	σS_{MW}	S/N
57955.75309	−18.17132	2.30	6.9634	4.6	−16.6	4.6	0.1838	0.0080	41.8
57955.91602	−18.17448	1.72	6.9752	3.4	−26.9	3.4	0.1939	0.0077	59.6
57956.72888	−18.17041	2.32	6.9676	4.6	−25.0	4.6	0.2022	0.0082	41.8
57956.91804	−18.17142	2.42	6.9667	4.8	−33.5	4.8	0.2255	0.0106	41.0
57957.89416	−18.17995	4.32	6.9690	8.6	−10.7	8.6	0.1634	0.0218	25.0
57959.78548	−18.17701	2.51	6.9612	5.0	−15.7	5.0	0.2194	0.0103	39.4
57959.90585	−18.17966	1.91	6.9555	3.8	−16.3	3.8	0.2075	0.0084	52.1
57960.74725	−18.18476	2.68	6.9651	5.4	−20.1	5.4	0.2090	0.0104	36.9
57960.84628	−18.18490	2.65	6.9605	5.3	−12.9	5.3	0.1981	0.0108	37.4
57961.76442	−18.17957	2.22	6.9582	4.4	−7.1	4.4	0.2149	0.0087	44.4
57961.83425	−18.18436	2.41	6.9526	4.8	−16.7	4.8	0.2094	0.0171	43.3
57962.78393	−18.17748	1.96	6.9541	3.9	−2.2	3.9	0.2119	0.0081	51.1
57962.87271	−18.19164	5.55	6.9251	11.1	−18.0	11.1	0.2266	0.0438	21.7
57964.74231	−18.17793	1.84	6.9650	3.7	−11.6	3.7	0.2149	0.0061	52.7
57964.83225	−18.18182	1.94	6.9492	3.9	−20.0	3.9	0.2078	0.0089	51.7
57965.73570	−18.19438	5.34	6.9277	10.7	−25.5	10.7	0.1945	0.0308	21.4
57965.83742	−18.18131	5.94	6.9409	11.9	−8.8	11.9	0.2740	0.0440	20.4
57993.66968	−18.18228	2.03	6.9482	4.1	−22.7	4.1	0.2104	0.0075	47.0
57993.78491	−18.17993	2.08	6.9523	4.2	−18.3	4.2	0.1954	0.0086	46.3
57993.84799	−18.18314	1.83	6.9520	3.7	−27.1	3.7	0.1934	0.0088	53.9
57994.63060	−18.17385	1.98	6.9446	4.0	−22.7	4.0	0.1980	0.0070	47.8
57994.74383	−18.17639	2.22	6.9466	4.4	−16.1	4.4	0.1864	0.0091	43.3
57994.82005	−18.17586	2.19	6.9553	4.4	−23.9	4.4	0.2004	0.0102	44.6
57995.63098	−18.17764	3.46	6.9558	6.9	−23.8	6.9	0.1701	0.0174	29.9
57998.62754	−18.19046	1.56	6.9459	3.1	−15.7	3.1	0.1987	0.0046	61.3
57998.71879	−18.19124	2.02	6.9506	4.0	−14.9	4.0	0.1797	0.0087	48.3
57998.81073	−18.18741	2.21	6.9488	4.4	−17.8	4.4	0.1645	0.0116	45.0
58008.66469	−18.18777	3.48	6.9314	7.0	−7.3	7.0	0.1958	0.0153	29.0
58010.65231	−18.19970	2.19	6.9277	4.4	−28.0	4.4	0.1689	0.0085	43.3
58010.77942	−18.19305	2.25	6.9234	4.5	−26.8	4.5	0.1921	0.0107	43.3
58010.83344	−18.19911	2.07	6.9391	4.1	−28.7	4.1	0.1985	0.0115	47.9
58011.68577	−18.18190	2.40	6.9283	4.8	−9.4	4.8	0.1728	0.0105	40.2
58011.77789	−18.18417	2.23	6.9321	4.5	−15.3	4.5	0.1739	0.0104	43.6
58011.83205	−18.18652	2.60	6.9261	5.2	−37.8	5.2	0.1888	0.0150	38.6
58012.67262	−18.18860	2.91	6.9347	5.8	−29.1	5.8	0.1680	0.0137	34.0
58012.75336	−18.19386	2.31	6.9312	4.6	−35.4	4.6	0.1780	0.0106	42.0
58012.82174	−18.18669	2.43	6.9230	4.9	−17.5	4.9	0.1579	0.0132	40.9
58013.67492	−18.18197	3.38	6.9334	6.8	−28.1	6.8	0.1733	0.0158	30.1
58013.74342	−18.18162	2.52	6.9295	5.0	−21.7	5.0	0.1862	0.0109	38.5
58013.81433	−18.18331	2.17	6.9467	4.3	−31.5	4.3	0.1964	0.0106	45.2
58014.68555	−18.18273	2.62	6.9207	5.2	−26.3	5.2	0.2481	0.0102	37.1
58014.77534	−18.18936	2.77	6.9302	5.5	−28.6	5.5	0.1661	0.0130	36.0
58018.63224	−18.18640	2.33	6.9479	4.7	−28.0	4.7	0.1890	0.0095	40.9
58018.72534	−18.18438	2.52	6.9262	5.0	−23.1	5.0	0.1978	0.0108	38.2
58019.62715	−18.19033	1.99	6.9432	4.0	−20.6	4.0	0.1888	0.0077	47.8
58019.72843	−18.19547	1.92	6.9260	3.8	−25.9	3.8	0.1963	0.0080	49.9
58020.66431	−18.18766	3.01	6.9468	6.0	−5.8	6.0	0.1870	0.0121	32.5
58020.75915	−18.18656	2.21	6.9431	4.4	−19.1	4.4	0.1977	0.0099	43.6
58021.55154	−18.17666	2.55	6.9344	5.1	−19.9	5.1	0.2109	0.0103	37.6
58021.66021	−18.18003	3.07	6.9414	6.1	−35.5	6.1	0.2225	0.0132	32.3
58021.75738	−18.18448	2.24	6.9325	4.5	−15.9	4.5	0.1845	0.0100	43.1
58022.53363	−18.18830	2.59	6.9472	5.2	−24.9	5.2	0.1947	0.0103	37.1
58022.59935	−18.18210	3.26	6.9427	6.5	−17.1	6.5	0.1937	0.0128	30.2
58022.74556	−18.19200	2.80	6.9414	5.6	−22.3	5.6	0.2040	0.0124	35.0
58023.53440	−18.17930	1.81	6.9489	3.6	−32.0	3.6	0.2030	0.0058	51.1
58023.63020	−18.17708	2.62	6.9523	5.2	−19.1	5.2	0.1963	0.0106	36.7
58023.75632	−18.18220	2.00	6.9325	4.0	−24.1	4.0	0.1824	0.0092	48.3

Table A.3. continued.

Time (BJD)	RV (km s^{-1})	σRV (m s^{-1})	*FWHM* (km s^{-1})	σ*FWHM* (m s^{-1})	BIS (m s^{-1})	σBIS (m s^{-1})	S_{MW}	σS_{MW}	S/N
58025.54957	−18.17300	1.67	6.9443	3.3	−17.9	3.3	0.2031	0.0055	56.1
58025.64932	−18.17642	1.82	6.9560	3.6	−19.6	3.6	0.1990	0.0074	52.8
58025.70429	−18.17085	1.93	6.9569	3.9	−4.2	3.9	0.2057	0.0089	50.3
58026.55716	−18.16496	4.02	6.9580	8.0	−8.4	8.0	0.2396	0.0170	25.7
58026.65617	−18.17836	2.73	6.9569	5.5	−22.0	5.5	0.2263	0.0112	35.7
58026.74871	−18.18277	2.88	6.9711	5.8	−22.1	5.8	0.1771	0.0154	35.2
58027.56593	−18.15614	5.14	6.9831	10.3	−11.8	10.3	0.2023	0.0274	21.8
58027.67900	−18.16790	4.30	7.0036	8.6	−8.0	8.6	0.1720	0.0246	25.4
58027.74799	−18.15559	5.45	6.9669	10.9	28.2	10.9	0.1827	0.0322	21.1
58041.54788	−18.19556	2.00	6.9314	4.0	−31.2	4.0	0.1730	0.0067	47.1
58043.56762	−18.18878	1.35	6.9287	2.7	−24.3	2.7	0.2094	0.0039	73.6
58043.72519	−18.18693	1.89	6.9299	3.8	−25.9	3.8	0.2145	0.0086	52.1
58052.55248	−18.18881	1.46	6.9380	2.9	−22.7	2.9	0.2180	0.0046	66.9
58052.61595	−18.19051	1.95	6.9391	3.9	−27.6	3.9	0.2350	0.0085	50.3
58053.56897	−18.18273	1.70	6.9377	3.4	−27.6	3.4	0.2239	0.0060	56.8
58053.64640	−18.18326	1.80	6.9436	3.6	−23.4	3.6	0.2202	0.0074	54.6
58054.52491	−18.18453	2.44	6.9497	4.9	−36.6	4.9	0.2112	0.0083	39.1
58054.67331	−18.18235	2.09	6.9612	4.2	−21.0	4.2	0.2261	0.0086	46.9
58056.53663	−18.18039	1.35	6.9497	2.7	−23.1	2.7	0.2132	0.0039	74.8
58056.62290	−18.18640	1.60	6.9600	3.2	−33.6	3.2	0.2198	0.0064	62.6
58057.53537	−18.18602	1.32	6.9511	2.6	−28.4	2.6	0.2202	0.0038	76.5
58057.59482	−18.18711	1.41	6.9528	2.8	−29.3	2.8	0.2291	0.0049	71.7
58068.58875	−18.18136	1.63	6.9330	3.3	−14.5	3.3	0.1845	0.0055	59.0
58069.65402	−18.19329	1.90	6.9399	3.8	−17.5	3.8	0.1783	0.0062	49.6
58070.66278	−18.19205	1.93	6.9408	3.9	−20.7	3.9	0.1868	0.0086	50.8
58071.54887	−18.18911	1.69	6.9187	3.4	−23.1	3.4	0.1924	0.0061	56.8
58074.55346	−18.18790	1.55	6.9236	3.1	−18.4	3.1	0.1788	0.0060	62.4
58075.53852	−18.18124	1.76	6.9243	3.5	−18.9	3.5	0.1630	0.0069	54.5
58077.54947	−18.18492	1.60	6.9297	3.2	−23.9	3.2	0.1872	0.0063	61.9
58079.61835	−18.19371	1.94	6.9281	3.9	−21.6	3.9	0.1803	0.0084	49.5

Table A.4. Parameters used in the analysis.

Parameter	Prior	Posterior Dartmouth (Adopted)	PARSEC
Stellar parameters			
Effective temperature $T_{\rm eff}$ (K)	$\mathcal{N}(5457, 29)$	5477 ± 27	5480 ± 24
Surface gravity log g (cgs)	$\mathcal{N}(4.42, 0.10)$	4.419 ± 0.053	4.429 ± 0.045
Iron abundance [Fe/H] (dex)	$\mathcal{N}(0.08, 0.02)$	0.078 ± 0.020	0.079 ± 0.020
Distance to Earth D (pc)	$\mathcal{N}(143.5, 10.9)$	145 ± 8	141 ± 6
Interstellar extinction $E(B-V)$ (mag)	$\mathcal{U}(0, 1)$	$0.009^{+0.011}_{-0.007}$	$0.009^{+0.011}_{-0.007}$
Systemic radial velocity γ (km s^{-1})	$\mathcal{U}(-20, -15)$	-18.186 ± 0.002	-18.186 ± 0.002
Linear limb-darkening coefficient u_a	(Derived)	0.4631 ± 0.0061	0.4625 ± 0.0057
Quadratic limb-darkening coefficient u_b	(Derived)	0.2270 ± 0.0041	0.2273 ± 0.0037
Stellar density $\rho_\star/\rho_\odot$	(Derived)	0.98 ± 0.19	1.03 ± 0.16
Stellar mass $M_\star$ ($M_\odot$)	(Derived)	0.915 ± 0.017	0.884 ± 0.018
Stellar radius $R_\star$ ($R_\odot$)	(Derived)	0.977 ± 0.053	0.950 ± 0.040
Stellar age τ (Gyr)	(Derived)	9.7 ± 3.0	10.8 ± 2.8
Planet b parameters			
Orbital period P (d)	$\mathcal{N}(2.369193, 0.01)$	$2.369172 \pm 8.9 \times 10^{-5}$	$2.369173 \pm 9.0 \times 10^{-5}$
Transit epoch T_0 (BJD - 2456000)	$\mathcal{N}(981.6425, 0.1)$	$981.6431 \pm 1.6 \times 10^{-3}$	$981.6431 \pm 1.6 \times 10^{-3}$
Radial velocity semi-amplitude K (m s^{-1})	$\mathcal{U}(0, 10^2)$	3.34 ± 0.43	3.33 ± 0.43
Orbital inclination i (°)	$\mathcal{S}(70, 90)$	87.7 ± 1.6	88.1 ± 1.4
Planet-to-star radius ratio k	$\mathcal{U}(0, 1)$	0.01604 ± 0.00041	0.01599 ± 0.00035
Orbital eccentricity e	$\mathcal{U}(0, 1)$	0.084 ± 0.079	0.080 ± 0.068
Argument of periastron ω (°)	$\mathcal{U}(0, 360)$	99^{+220}_{-77}	94^{+220}_{-71}
System scale $a/R_\star$	(Derived)	7.43 ± 0.45	7.56 ± 3.8
Impact parameter b	(Derived)	0.30 ± 0.20	0.25 ± 0.19
Transit duration T_{14} (h)	(Derived)	2.266 ± 0.050	2.264 ± 0.049
Semi-major axis a (AU)	(Derived)	0.03376 ± 0.00021	0.03337 ± 0.00023
Planet mass $M_{\rm p}$ ($M_\oplus$)	(Derived)	6.54 ± 0.84	6.38 ± 0.83
Planet radius $R_{\rm p}$ ($R_\oplus$)	(Derived)	1.71 ± 0.11	1.654 ± 0.84
Planet bulk density $\rho_{\rm p}$ (g cm^{-3})	(Derived)	7.1 ± 1.8	7.7 ± 1.7
Gaussian process hyperparameters			
A (m s^{-1})	$\mathcal{U}(0, 100)$	$6.0^{+1.3}_{-0.8}$	5.96 ± 1.2
λ_1 (d)	$\mathcal{U}(0, 100)$	34 ± 12	34 ± 12
λ_2	$\mathcal{U}(0, 10)$	0.46 ± 0.12	0.46 ± 0.12
$P_{\rm rot}$ (d)	$\mathcal{N}(32.2, 0.6)$	32.2 ± 0.5	32.2 ± 0.5
Instrument-related parameters			
HARPS jitter (m s^{-1})	$\mathcal{U}(0, 10^2)$	1.9 ± 0.4	1.9 ± 0.4
K2 contamination (%)	$\mathcal{N}_{\mathcal{U}}(0.952, 0.024, 0, 100)$	0.952 ± 0.024	0.952 ± 0.024
K2 jitter (ppm)	$\mathcal{U}(0, 10^5)$	59 ± 1	59 ± 1
K2 out-of-transit flux	$\mathcal{U}(0.99, 1.01)$	$1.000006 \pm 2 \times 10^{-6}$	$1.000006 \pm 2 \times 10^{-6}$
SED jitter (mag)	$\mathcal{U}(0, 0.1)$	0.054 ± 0.021	0.054 ± 0.022

Notes. The respective priors are provided together with the posteriors for both the Dartmouth and PARSEC stellar evolution tracks. The posterior values represent the median and 68.3% credible interval. Fixed and derived values that might be useful for follow-up work are also reported. $\mathcal{N}(\mu, \sigma^2)$: normal distribution with mean μ and width σ^2. $\mathcal{U}(a, b)$: uniform distribution between a and b. $\mathcal{N}_{\mathcal{U}}(\mu, \sigma^2, a, b)$: normal distribution with mean μ and width σ^2 multiplied with a uniform distribution between a and b. $\mathcal{S}(a, b)$: sine distribution between a and b.